



# X-Ray Stereo Digital Image Correlation

E.M.C. Jones<sup>1</sup> · E.C. Quintana<sup>1</sup> · P.L. Reu<sup>1</sup> · J.L. Wagner<sup>1</sup>

Received: 4 February 2019 / Accepted: 24 July 2019 / Published online: 26 August 2019  
© The Society for Experimental Mechanics, Inc 2019

## Abstract

Digital Image Correlation (DIC) is a well-established, non-contact diagnostic technique used to measure shape, displacement and strain of a solid specimen subjected to loading or deformation. However, measurements using standard DIC can have significant errors or be completely infeasible in challenging experiments, such as explosive, combustion, or fluid-structure interaction applications, where beam-steering due to index of refraction variation biases measurements or where the sample is engulfed in flames or soot. To address these challenges, we propose using X-ray imaging instead of visible light imaging for stereo-DIC, since refraction of X-rays is negligible in many situations, and X-rays can penetrate occluding material. Two methods of creating an appropriate pattern for X-ray DIC are presented, both based on adding a dense material in a random speckle pattern on top of a less-dense specimen. A standard dot-calibration target is adapted for X-ray imaging, allowing the common bundle-adjustment calibration process in commercial stereo-DIC software to be used. High-quality X-ray images with sufficient signal-to-noise ratios for DIC are obtained for aluminum specimens with thickness up to 22.2 mm, with a speckle pattern thickness of only 80  $\mu\text{m}$  of tantalum. The accuracy and precision of X-ray DIC measurements are verified through simultaneous optical and X-ray stereo-DIC measurements during rigid in-plane and out-of-plane translations, where errors in the X-ray DIC displacements were approximately 2–10  $\mu\text{m}$  for applied displacements up to 20 mm. Finally, a vast reduction in measurement error—5–20 times reduction of displacement error and 2–3 times reduction of strain error—is demonstrated, by comparing X-ray and optical DIC when a hot plate induced a heterogeneous index of refraction field in the air between the specimen and the imaging systems. Collectively, these results show the feasibility of using X-ray-based stereo-DIC for non-contact measurements in exacting experimental conditions, where optical DIC cannot be used.

**Keywords** Digital Image Correlation (DIC) · Index of refraction · X-ray

## Introduction

Digital Image Correlation (DIC) is a powerful, image-based diagnostic tool for measuring the shape, displacement and deformation of an object [1]. A pattern on the surface of the specimen is imaged periodically while the specimen is subjected to some type of loading. The pattern consists of random light and dark features, and can be either the natural object surface, or can be applied using techniques such as incomplete layers of white and black spray paint. Using the principle of optical flow, DIC tracks the motion of the pattern through consecutive images. Two-dimensional DIC (2D-DIC) is the simplest category of DIC, in which

a single camera is mounted perpendicular to a planar object. The displacement and deformation of the object are restricted to a plane perpendicular to the optical axis, and only in-plane displacements are measured. An extension of 2D-DIC is stereo-DIC (S-DIC), in which two cameras are mounted at a stereo angle viewing the same region of interest on the object. By using *a priori* knowledge of the geometry of the stereo-rig (obtained through the stereo-system calibration routine), S-DIC provides three-dimensional shape and deformation measurements of the surface of the object. Compared to 2D-DIC, S-DIC is generally preferred, since it eliminates the planar restriction and perspective error for objects moving towards or away from the cameras.

Since the initial presentation of 2D-DIC in the early 1980s [2], DIC has matured significantly and is now a well-established diagnostic technique. The International Digital Image Correlation Society (iDICs) has even begun the process of standardizing DIC for simple applications,

✉ E.M.C. Jones  
emjones@sandia.gov

<sup>1</sup> Sandia National Laboratories, Albuquerque, NM, USA



such as mechanical characterization of materials in a standard laboratory environment [3]. As DIC becomes more common, however, researchers are pushing DIC into more complex test environments that add significant challenges to making precise and accurate DIC measurements. For example, in explosive or combustion research, the sample may be engulfed in flames or smoke and be visually occluded, making optical-based measurements difficult or impossible [4]. Another formidable challenge, which is the focus of the current work, involves index of refraction variations (either spatial or temporal) of the medium through which the object is imaged. This situation can occur in many different experiments, such as: (1) The object is heated, and temperature- and density-gradients develop in the air between the object and the camera [5–7]; (2) The object is in an explosive environment and shock waves pass between the object and the camera [8–11]; (3) The object is in a wind tunnel or shock tube and is imaged through a complex fluid flow [12, 13]. In all of these situations, visible light is refracted through density gradients in the medium(s) between the object and the camera, leading to beam-steering effects which manifest as false displacements and strains in DIC measurements. The magnitude of the errors depends on the optical setup, but can be on the order of 0.5 pixels or 220  $\mu\text{m}$  of false displacements and 5000  $\mu\text{m m}^{-1}$  of false strains induced by heat waves [5], and 10–50  $\mu\text{m}$  of false displacements induced by a shock wave [11]. These errors are much larger than the resolution expected of DIC measurements in a well-controlled environment.

To address these issues, we propose using X-ray imaging in place of optical imaging for S-DIC. Compared to visible light, diffraction of X-rays through the density gradients of interest are negligible [14–16], and X-rays can penetrate occluding material. The concept of X-ray based stereo-DIC (XS-DIC) is a straight-forward extension of optical S-DIC. Instead of two cameras that image visible light reflected from the surface of the specimen, two X-ray detectors capture X-ray photons that pass through the object. The intensity or grey-level values of the X-ray images represent the local radiodensity of the object, integrated over the total path length, with dark and light pixels corresponding to areas with greater or lower X-ray attenuation, respectively. The amount of X-ray energy that is absorbed by a material depends on the X-ray energy, mass absorption coefficient of the material, the density of the material, and the object thickness [17]. Thus, one approach for creating a pattern for XS-DIC is to apply a thin layer of a dense material in a random pattern onto the surface of a less-dense object. This is analogous to applying white and black paint speckles to the surface of an object to create a pattern for optical DIC. Unique to XS-DIC, though, is that the pattern can be applied on a surface that is not optically visible, e.g. on an interior surface of a component of an assembly. Similar

to optical DIC, this pattern is imaged periodically while the object is loaded, and successive images are correlated to produce full-field shape, displacement and deformation measurements in three dimensions of the patterned surface.

Previously, 2D-DIC has been performed with X-ray based images, which we refer to here as X2D-DIC.<sup>1</sup> Russell and Sutton [18] measured the in-plane strain of a glass-epoxy composite. They created a pattern for X2D-DIC by applying stainless-steel metal powder onto the surface of the composite with a lacquer binder. They only reported strains on the visible surface, but proposed that internal strain fields could also be investigated by seeding steel particles in between the composite layers during manufacturing. A group of researchers from the University of Cambridge, including Grantham, Goldrein, Proud, and Field among others, have applied X2D-DIC to numerous applications [19–21]. In all of these cases, the test object was seeded on an internal plane with high-density, X-ray opaque particles to create a speckle pattern. X-ray images were captured before and after deformation, and a cross-correlation matching criterion was used to measure 2D displacements of the seeded plane. Rae et al. [22] seeded a plane with two types of lead particles, sandwiched in the middle of a cylindrical mock explosive, and used a flash x-ray system to image the test object at one instance in time while it was penetrated by a projectile at approximately 500  $\text{m s}^{-1}$ . They evaluated three different correlation algorithms and found that for all three algorithms, the sub-optimal speckle pattern necessitated large subset sizes (approximately  $101 \times 101$  pixels<sup>2</sup>), which decreased the spatial resolution and data density of the measurements. As an alternative to seeding a specific plane, Louis et al. [23] and Bay [24] used radiographs of heterogeneous samples as a pattern for DIC. The dark and light regions of the pattern were functions of the total X-ray absorption through the entire thickness of the specimen. In these cases, the 2D displacement and strain fields they computed were averages through the thickness of the object. Additionally, Bay compared the strain fields from X2D-DIC with strain fields computed from particle tracking on the surface of the specimen, and showed that when the resolutions of the two techniques were matched, the measurements were quantitatively and qualitatively similar. Finally, Synnergren et al. [25] performed XS-DIC on a polyester specimen seeded on an internal plane with lead particles, where two X-ray heads and detectors each viewed the specimen from a different angle. They used cross-correlation between the reference and deformed images for each X-ray system to obtain apparent 2D displacements in each system. The computation of 3D displacements from the apparent 2D

<sup>1</sup>In the literature, X2D-DIC has also been called “digital speckle photography”, “digital speckle radiography”, or “texture correlation”.



displacements required careful measurement with a ruler to determine the geometry of the two systems.

Volumetric-DIC, also called Digital Volume Correlation (DVC), is another related diagnostic that is also based on X-ray imaging [1, 26]. However, there are several key differences that distinguish XS-DIC from DVC. First, DVC provides measurements throughout the entire volume of the object, while XS-DIC provides measurements only on the surface of the object that is patterned. In this respect, DVC is advantageous over XS-DIC. Second, DVC requires a pattern throughout the entire volume of the object, while XS-DIC requires a pattern only on a single surface. For homogeneous specimens, creating a pattern for DVC requires an invasive alteration of the object, e.g. the addition of particles of a dense material to a less-dense polymer, which typically results in radically different material properties. Therefore, the test object for DVC is typically restricted to naturally heterogeneous composites or porous materials [27], and sub-optimal natural patterns or patterns that degrade during deformation can lead to decorrelation and/or measurement errors [28]. Applying a pattern on a single surface for XS-DIC, though, is less invasive, and thus XS-DIC is applicable to homogeneous objects. Third, DVC is applicable only to static tests where loading is applied in isolated steps, since some form of time-intensive volumetric imaging of the object is required at each load step (e.g. collection of a series of 2D images at varying rotational angles around the object). In contrast, XS-DIC can be used in dynamic tests, since only a single pair of X-ray images is required for each instance in time.

In this paper, we describe a novel approach for XS-DIC, and provide a thorough comparison to optical S-DIC. First, we detail several techniques for creating an appropriate pattern for XS-DIC, including a unique method using thermal spray coating to create a thin and unobtrusive pattern. Next, we describe how the common bundle-adjustment calibration routine for optical S-DIC can be adapted for XS-DIC, making our approach more streamlined and compatible with commercial DIC software compared to previous works. Next, we evaluate the X-ray image quality for different patterns and different thicknesses of samples. Using simple translation tests, we compare the accuracy and precision of XS-DIC to standard optical S-DIC, by performing both XS-DIC and S-DIC simultaneously. Finally, we induce a heterogeneous index of refraction field by placing a hot plate between the sample and the imaging systems, and show a vast reduction in false displacements and strains with the X-ray system compared to the optical system.

The viability of XS-DIC is demonstrated here with a simplified experimental setup, where beam steering is caused by a hot plate, quasi-static image acquisition rates of 5 Hz or less are used, and the surface of interest of the test

piece is on the exterior and optically visible. However, our target application for XS-DIC is to measure the response (i.e. displacement, velocity, and strain measured directly with DIC, as well as full-field mode shape, mode amplitude, and damping derived from the DIC measurements) of a jointed structure subjected to fluid loading in a shock tube [11]. In this target application, beam steering is caused by imaging through a shock front and turbulent fluid flow, dynamic image acquisition rates of 10–20 kHz are required, and the surface of interest is in the interior of an assembly. The current work lays the foundation for using XS-DIC in this complicated fluid-structure interaction application, and more generally for non-contact measurements of shape, displacement and strain in challenging experiments, where optical access is not possible or where index of refraction variations add significant bias to optical S-DIC measurements.

## Experimental Methods

### Speckle Patterning Techniques

There are three main requirements of a speckle pattern for DIC [3]:

- The pattern must adhere to the specimen so that deformation of the pattern reflects deformation of the underlying material of interest.
- The pattern must have significant contrast in intensity.
- The pattern must be sufficiently unique (e.g. random and non-periodic) so that one subset or facet can be correlated from one image to the next.

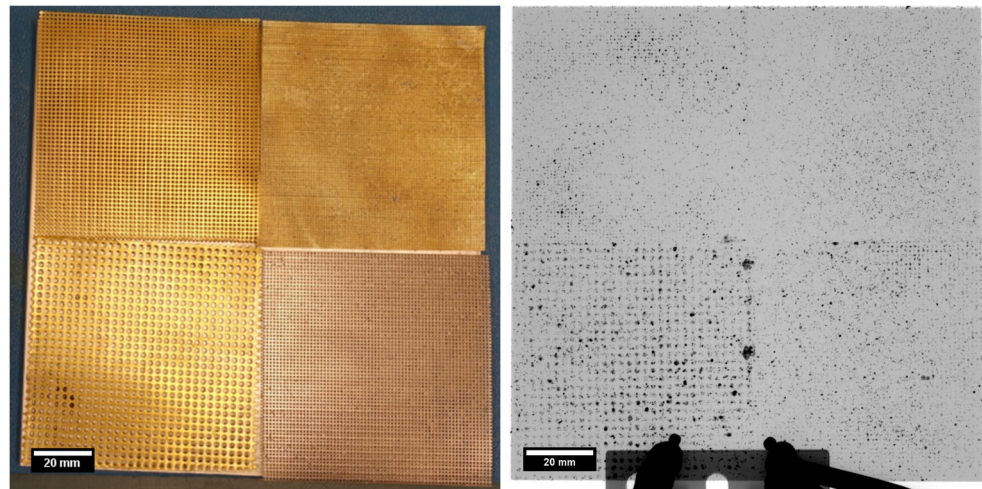
In optical-based DIC, speckle patterns are created in a variety of ways, depending on the length scale of interest. One of the most common speckling techniques is a base layer of white paint followed by some sort of black speckles, such as an incomplete layer of black spray paint, black paint applied through a mask with specific sized holes, an ink applied with a stamp, Sharpie marker applied by hand, carbon powder sprinkled onto the wet white paint, etc. The key to all of these variations is that the white background and black speckles create good intensity contrast in the images of the speckle pattern.

For X-ray-based DIC, intensity contrast in the images depends on the local X-ray attenuation, integrated over the total path length or specimen thickness. X-ray attenuation, in turn, is a function of X-ray energy, mass absorption coefficient of the material(s), and the density of the material(s) [17]. When designing a pattern for DIC, one goal is to minimize the impact the pattern has on the specimen response. Given aluminum specimens, we sought to create thin speckles using dense metals, such as tungsten





**Fig. 1** (Left) Four different-sized wire meshes through which a mixture of tungsten powder and paint was applied to create an X-ray DIC speckle pattern on an aluminum specimen. (Right) X-ray image of the resulting DIC pattern on the specimen



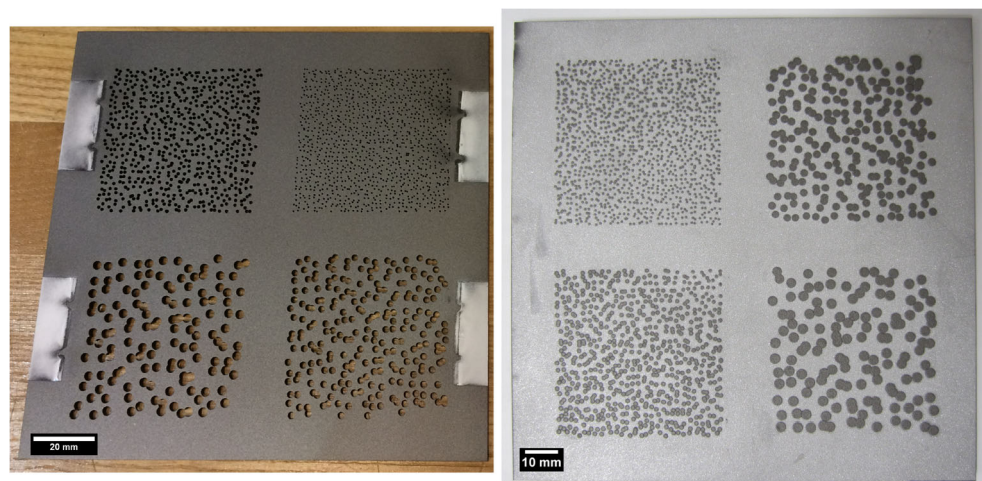
or tantalum. In this way, the X-rays are attenuated more in the dense speckles than in the background aluminum specimen, and the speckles appear darker than the rest of the specimen.

We explored two different speckling techniques. First, we mixed tungsten powder in paint, and then applied the mixture to the aluminum specimens (140 × 140 mm, 3.18 mm thick) in a variety of ways, including flicking a paint brush saturated with the mixture, painting through wire meshes of different sizes, painting through a mask of holes drilled in random locations, and hand-painting individual speckles with a fine-point paint brush. Figure 1 shows an example of four different-sized meshes we painted through and the resulting speckle patterns. In general, there is decent contrast, but the speckle size and contrast are not consistent, and all of the different application methods are cumbersome. However, we believe some variation of the application method could be refined, and that tungsten powder mixed in paint could be a viable, inexpensive speckling technique.

Instead of focusing on refining the tungsten powder in paint technique, we pursued a second option for creating a speckle pattern of a dense metal using thermal spray coating. In brief, the principle of thermal spray coating [29, 30] is to pass a powder of the coating material through a heat source in order to soften or melt it. The softened or molten material is then propelled by process gases towards the base material. Upon impact, the particles rapidly quench and solidify, forming pancake-like structures, often called “splats”. Over time, a nominally solid coating is built that has a complex micro-structure, including porosity, micro-cracks, oxidation from entrained air, and varying structures of the coating material arising from unmelted, partially-melted, and fully melted splats. Adhesion between the coating and the base material is mechanical (opposed to chemical), and adhesion between layers of the coating is based on mechanical interlocking of the splats.

To use thermal spray to create an X-ray DIC speckle pattern, we first created a mask of randomly-located holes milled into an aluminum blank (1.59 mm thick), as shown

**Fig. 2** (Left) Mask of randomly-located holes used for the thermal spray patterning. (Right) Optical image of the pattern created by thermal spray of Ta powder on an Al specimen



in Fig. 2. We chose four different hole sizes, nominally 0.5 mm, 1 mm, 2 mm and 3 mm diameter, in order to evaluate the efficacy of the process to create different sized speckles. The locations of the holes were generated using the “Speckle Generator” program provided by Correlated Solutions, and the holes were milled using computer-numerical-control (CNC) machining. The density of the holes (and thus the speckles) was chosen to be sparse, so that the diameter and thickness of individual speckles could be measured to evaluate the fidelity of the final speckle size with respect to the initial mask hole size.

The exemplar specimen was an aluminum blank (140 × 140 mm, 3.18 mm thick), which was sandblasted to promote adhesion between the aluminum and the applied coating. The mask was offset from the specimen using shims by either 3.18 mm (specimen 1) or 0.38 mm (specimen 2). Tantalum powder was then thermally sprayed through the mask onto the aluminum specimen, using the parameters shown in Table 1. Afterward, the specimens were cleaned using ethanol to remove loose Ta powder that was not adhered to the specimen. Figure 2 shows an optical image of the final specimen with the Ta-based DIC speckle pattern.

The thickness of the coating was measured using an optical profilometer (Keyence, VR3200, 40X magnification, fine scan), which provided a 2D, full-field map of the height of the specimen. Two regions (ca. 7.6 × 5.7 mm) of each quadrant were scanned, and the speckles were identified either manually (Specimen 1) or by thresholding the height data (Specimen 2). The heights of the speckles were then averaged and subtracted from the mean height of the background to estimate the thickness of the coating. The diameters of the speckles were estimated using a “blob analysis” of X-ray images of the specimens [31]. Both the thickness and diameter results for each quadrant of each of the two specimens are shown in Table 2.

**Table 1** Parameters used in the thermal spray coating

Parameter	Value
Powder	H.C. Starck Amperit 150.074 Tantalum
Torch	Triplex 210 Pro
Nozzle size	11 mm
Powder injector size	2 mm
Powder injector ring angle	105°
Injector Ring annular position	40°
Air cooling	Silvent, 40 bar
Powder carrier gas	Argon, 3 liter/minute
Plasma gas (primary)	Argon, 48 liter/minute
Plasma gas (adjunct)	Helium, 12 liter/minute
Current	475 amps
Powder feed rate	20 gram/minute

**Table 2** Properties of X-ray speckle made via thermal spray coating

Mask Hole Size (mm)	Speckle Diameter (mm)		Speckle Thickness (μm)	
	Specimen 1	Specimen 2	Specimen 1	Specimen 2
0.5	0.7 +/- 0.1	0.6 +/- 0.1	8.0	79.7
1.0	1.0 +/- 0.2	0.9 +/- 0.2	12.9	88.2
2.0	1.7 +/- 0.4	1.7 +/- 0.2	15.8	89.8
3.0	1.9 +/- 0.7	2.1 +/- 0.3	15.1	85.1

While the specimens consisted of four quadrants with different sized speckles in each quadrant, we focused only on the smallest speckles, nominally 0.5 mm diameter. The effect of the ratio of Ta to Al thickness on the X-ray images was explored by stacking various numbers of blank Al plates behind the specimens, making the total thickness of Al through which the X-rays had to pass either 3.2 mm (no extra plates), 12.7 mm (3 extra plates), or 22.2 mm (6 extra plates). The specimen designations are detailed in Table 3.

For the optical DIC system, a digital file (Portable Document Format or PDF) was created as the inverse of the hole pattern that was used to generate the mask for the thermal spray coating. This PDF speckle pattern was printed on adhesive label paper using a laser printer<sup>2</sup> and adhered to the front of the specimen, directly on top of the Ta X-ray pattern. The two patterns were aligned manually. The thin paper and ink for the optical speckle pattern was completely transparent to the X-rays and did not affect the X-ray images. Thus, optical images of the printed speckle pattern could be captured simultaneously with X-ray images of the Ta thermal spray pattern, as described in “Stereo Imaging Systems”.

## Stereo Imaging Systems

In order to evaluate X-ray-based DIC, we set up a system to perform simultaneous optical imaging and X-ray imaging of the same specimen, as shown in Fig. 3. Table 4 summarizes the equipment. Two X-ray machines were mounted at a stereo angle in front of the specimen, and two X-ray detectors were placed behind the specimen. Two optical cameras were mounted above the X-ray machines, pointing down at the specimen at a stereo angle. The specimen was

<sup>2</sup>Laser-printed patterns on paper can suffer from dithering, where the borders of the speckles are polluted by small droplets of ink. In some situations, this can cause spatial aliasing in digital images of the speckle pattern. However, these spurious features were measured with a high-magnification, high-resolution image to be approximately 85 μm or smaller. Additionally, the lens system resolution was measured to be 7 lp/mm, which translates to a smallest resolvable feature of 70 μm. Therefore, the lens acts as an analog filter, filtering the small features on the edges of the speckles, leading to unaliased speckles in the images used for optical DIC.



**Table 3** Specimen configurations

Specimen name	Ta coating thickness ( $\mu\text{m}$ )	Aluminum thickness (mm)	Ta/Al thickness ratio ( $\cdot 10^{-3}$ )
A	79.7	3.2	25.1
B	79.7	12.7	6.3
C	79.7	22.2	3.6
D	8.0	3.2	2.5
E	8.0	12.7	0.6

illuminated for optical images with halogen lights placed behind and above the cameras. Both imaging systems were set to have approximately the same field of view, centered on the quadrant with the smallest speckles (nominally 0.5 mm diameter). Because the Ta speckles created with the thermal spray system were slightly larger than the nominal hole diameter of the mask (Table 2), and because the image scale was slightly larger in the X-ray system, the speckles were slightly larger in the X-ray images compared to the optical images. This effected the subset size as described in “DIC Processing Parameters”. Images from all four systems (two X-ray detectors and two optical cameras) were synchronized manually, which was sufficient for static testing.

### Camera Calibration

An essential component to stereo-DIC is determining the intrinsic parameters of the imaging system (i.e. focal length, center of sensor, skew) and extrinsic parameters of the stereo system (i.e. translation and rotation of each imaging system to the world coordinates). For standard, optical-based DIC, the user captures images of the surface of a calibration target as the target is rotated and translated within the volume of interest. Typically, the calibration targets are planar or bi-level, and have some features, such as an array of dots, that are at known locations on the surface of the target. Commercial DIC software is then used to extract the location of the features in each image and triangulate

in order to determine the location of the features in 3D space. Finally, a bundle adjustment optimization process is used to determine the intrinsic and extrinsic parameters simultaneously [1].

To calibrate a stereo X-ray system, two methods were proposed and evaluated by Miller and Quintana [32]. The first method involved capturing a single pair of images (one image from each X-ray system) of a three-dimensional calibration target. The second method mimicked the approach used by commercial (optical) DIC software, by capturing many pairs of images as a planar calibration target was rotated and translated within the volume of interest.

For this work, we followed the second approach. A dot-grid calibration target suitable for both X-ray and optical imaging was fabricated using printed circuit-board processes, where gold dots of 2.5 mm diameter were etched in a  $9 \times 9$  array with 5 mm spacing on the printed circuit board substrate. On top of the gold dots, white plastic dots were printed with black plastic filling in the background. In the X-ray images, the dense gold dots appeared dark while the plastic provided a light background. In the optical images, the contrast is reversed, with the white plastic dots appearing light against a dark background. Thus, a single calibration target was imaged simultaneously with both the X-ray and the optical stereo DIC systems (Fig. 4). While the images for the two stereo systems were captured simultaneously, the calibration process (i.e. determination of the intrinsic and extrinsic parameters) was done independently for each system.

The calibration target was mounted on a 3-axis motorized translation stage and a 1-axis motorized rotation stage, both of which could be operated remotely, as well as a 1-axis manual tilt stage. The target was initially mounted perpendicular to the X-ray system at the center of the depth of field, and it was first rotated about the vertical axis in  $5^\circ$  increments to  $\pm 35^\circ$ . Then it was returned to center and translated vertically and horizontally in 10 mm increments so that it filled the field of view of all four cameras. Next, it was plunged out-of-plane in 5 mm increments to  $\pm 20$  mm. Finally, the target was tilted back so that it was approximately perpendicular to the optical cameras, and the

**Fig. 3** Experimental setup used for simultaneous optical and X-ray imaging

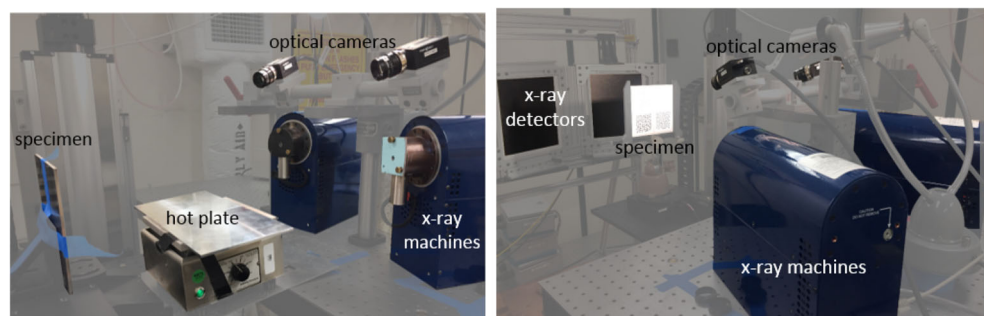




**Table 4** Experimental equipment for X-ray and optical imaging

	Optical DIC	X-ray DIC
X-ray Machine	N/A	Kevex PXS10-65W
Camera or Detector	2.3 MP PointGrey Grasshopper	Varex 2520DX, CsI
Lens	35 mm (Schneider)	N/A
Stereo-Angle (approximate)	33 deg.	28 deg.
Accelerating Voltage	N/A	130 kV
Current	N/A	0.5 mA
Spot Size	N/A	100 $\mu\text{m}$
Exposure or Integration Time	25 ms	200 ms
Field-of-View (approximate)	55 $\times$ 55 mm <sup>2</sup>	55 $\times$ 55 mm <sup>2</sup>
Image Resolution	1920 $\times$ 1200 px <sup>2</sup>	1536 $\times$ 1920 px <sup>2</sup>
Image Scale (approximate)	12.1 px/mm	16.4 px/mm
Speckle Diameter (approximate)	0.5 mm / 6 px	0.7 mm / 11 px

above rotations and translations were repeated, though with larger increments.

The optical images were captured as 8-bit images, and no further post-processing was done. The X-ray images were initially captured as 16-bit raw images, and then a flat-field image correction was applied. For the X-ray image acquisition, the detector was operated at 5 frames per second, and a 16-frame average was used to achieve a higher signal-to-noise ratio. A histogram equalization was then applied, and the images were scaled to 8-bit images. Finally, the two stereo-DIC systems were independently calibrated using Vic-3D (Correlated Solutions), with a standard pin-hole camera model and a third-order radial lens distortion model.

We stress that this calibration procedure is compatible with commercial DIC software, and thus no modifications or custom software are necessary to use X-ray images in lieu of optical images. This is in contrast to previous works, such as [25], which required a manual measurement

of the position of the X-ray sources and detectors for calibration. By using procedures that interface seamlessly with commercial DIC software, our method of XS-DIC is more easily realized.

### Translation Tests

The first test we used to evaluate the precision and accuracy of XS-DIC was a specimen undergoing rigid translations. The specimen was mounted to a motorized, nano-precision translation stage (Aerotech, ANT130-XY). Using the stage, the specimen was translated first horizontally in steps of 10  $\mu\text{m}$  up to a total displacement of 50  $\mu\text{m}$ , then in steps of 4 mm up to a total displacement of 16 mm (Motion 1). The stage was then returned to its home position (Motion 2). Next, the specimen was translated away from the optical cameras and X-ray machines in increments of 4 mm up to a total displacement of  $-20$  mm (Motion 3), returned to home (Motion 4), translated towards the

**Fig. 4** Calibration target used for both the X-ray and the optical stereo DIC systems. (Left) Example image of the calibration target captured by the optical system. (Right) Example image of the calibration target captured by the X-ray system

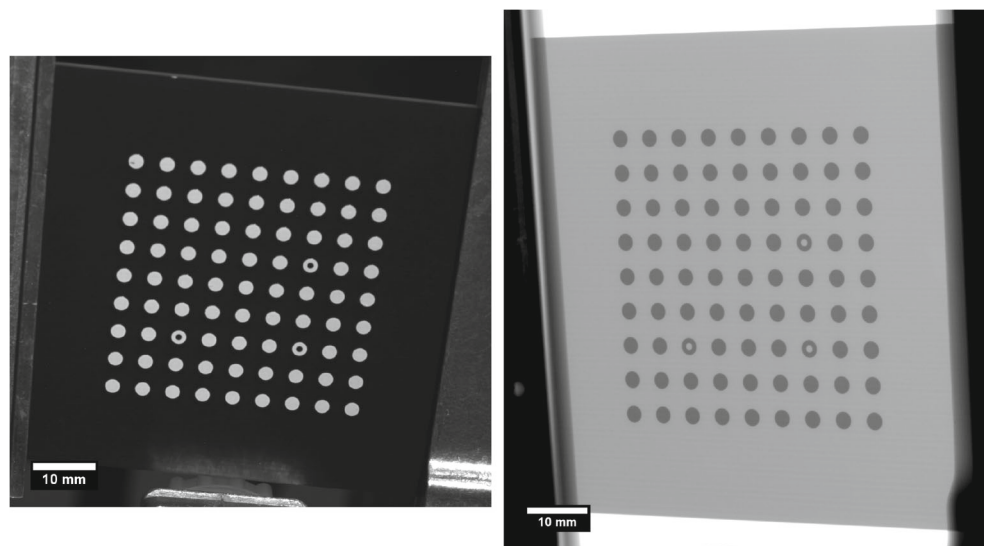


**Table 5** DIC settings used for optical and X-ray images

DIC Software	Correlated Solutions, Vic-3D
Image Pre-Filtering	Default low-pass filter
Subset Size	$35 \times 35 \text{ px}^2$ (Optical) / $43 \times 43 \text{ px}^2$ (X-ray)
Step Size	10 px
Interpolant	8-tap
Subset Shape Function	Affine
Correlation Criterion	Zero-normalized sum of squared differences (ZNSSD)
Strain Formulation	Green-Lagrange
Strain Window	5 data points
Virtual Strain Gauge Size <sup>a</sup>	75 px or 6.2 mm (Optical) / 83 px or 5.1 mm (X-ray)

<sup>a</sup>The VSG size is approximated as  $L_{VSG} = (L_{window} - 1)L_{step} + L_{subset}$ , where  $L_{VSG}$  is the VSG size in pixels,  $L_{window}$  is the strain window in data points,  $L_{step}$  is the step size in pixels, and  $L_{subset}$  is the subset size in pixels [3]

cameras in increments of 4 mm up to a total displacement of 20 mm (Motion 5), and finally returned home again (Motion 6). At each position, the specimen was kept stationary while an image was captured in both the X-ray and the optical systems. These translations were performed for each specimen configuration listed in Table 3.

Similar to the images of the calibration target (Camera Calibration), the optical images were captured as 8-bit images, and no further post-processing was done. The X-ray images were captured as 16-bit raw images, a flat-field image correction was applied, and 16 frames were averaged together. However, no histogram equalization was performed, and the images were retained as 16-bit images.

### Hot Plate Tests

As mentioned previously, the main motivation for developing X-ray based DIC was to be able to use DIC in harsh environments, in which density gradients in the atmosphere refract visible light and severely distort optical DIC measurements. While the actual application of interest is high-speed flows such as in a shock tube or wind tunnel, we induced density gradients in the air in the current mock experiment by placing a hot plate between the specimen and the optical cameras and X-ray machines, as shown in Fig. 3.

The center of the hot plate (Sybron Thermolyne Model HP-A1915B) was located approximately 46 cm from the optical cameras and approximately 7.5 cm from the specimen, and the top of the hot plate was approximately aligned with the bottom of the quadrant of interest of the specimen. The top surface of the hot plate was approximately  $15 \times 15 \text{ cm}$ , but two aluminum plates were placed on top of it in order to increase the effective width of the heated area to approximately 28 cm. This was done to ensure that the FOV of each imaging system was looking through the region of air affected by heat waves above the hot plate.

The temperature of the hot plate was increased until the optical images were visually shimmering due to the heat waves. Both optical and X-ray images of the specimen were captured at approximately 5 Hz over a 40 s period. A flat-field image correction was applied to the X-ray images, but no frame averaging was performed. The specimen remained stationary during this time, so any DIC measurements from these images are false displacements and strains caused by refraction through the heat waves.

### DIC Processing Parameters

The optical and the X-ray DIC images were processed using the settings in Table 5 to compute full-field displacements and strains. The subset size was selected based on having at least three speckles per subset, as recommended by the *Good Practices Guide for Digital Image Correlation* [3]. Figure 5 shows a representative subset for the optical images and for Specimen A of the X-ray images. This criterion led to a slightly larger subset for the X-ray system ( $43 \times 43 \text{ px}^2$ ) compared to the optical system ( $35 \times 35 \text{ px}^2$ ) because the speckles were larger in the X-ray images compared to the

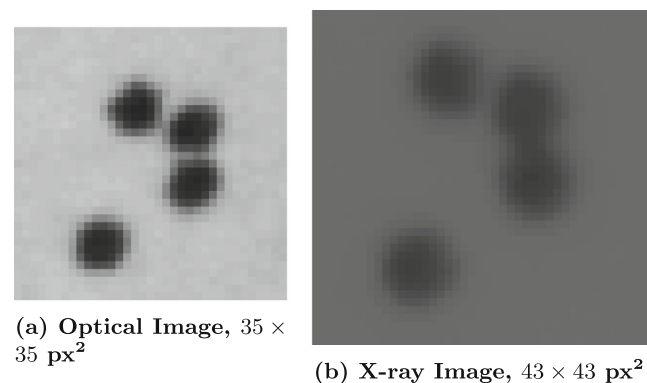


**Fig. 5** Representative subsets for the optical images and the X-ray images (Specimen A)



optical images (Table 4). Additionally, the subsets for both systems were relatively large because the density of the speckles was low. The speckle density was purposefully designed to be sparse for the current work, because we wanted to evaluate the fidelity of the final speckle size with respect to the hole size in the mask when using the thermal spray coating technique. However, moving forward, a mask with a higher hole density pattern could easily be fabricated, resulting in a DIC speckle pattern with closer to the recommended 50% speckle coverage [3]. A denser pattern would be critical for measurements with high spatial gradients in the displacements and strains [22]. Alternatively, a higher-order subset shape function (e.g. quadratic instead of affine) could be used if larger subsets are required [3]. However, for the rigid translation tests used in this work, with no spatial gradients in displacements or strains, large subsets with an affine shape function were acceptable. Smaller subsets— $27 \times 27$  px<sup>2</sup> for the optical system and  $33 \times 33$  px<sup>2</sup> for the X-ray system—produced the same mean displacements but with slightly higher noise.

For the rigid translation tests, one reference image was used for the set of in-plane translations (Motions 1–2), and a second reference image was used for the set of out-of-plane translations (Motions 3–6). For the hot plate tests, a single reference image collected at the beginning of the image series was used.

## Results and Discussion

### X-ray Image Quality

Figure 6 shows X-ray images of the different specimen configurations, with different thicknesses of Ta and Al (Table 3). For comparison, an optical image of the printed speckle pattern adhered on top of the X-ray pattern is also shown. The left column shows the actual image intensities on a reduced range of the 16-bit X-ray images; for the right column, the image intensities were rescaled so that they ranged from 0–255 on an 8-bit scale, thus leading to constant contrast for each image. The successive addition of more aluminum between specimens A, B, and C caused the image to darken and the contrast to be reduced; a similar trend was observed between specimens D and E. The thinner Ta speckle pattern of specimens D and E was less sharp and had much less contrast and more noise than the thicker Ta speckle pattern of specimens A, B, and C.

The mean intensity, image contrast, and image noise are shown in Fig. 7 as a function of the ratio of Ta to Al thicknesses. Image contrast is defined as the difference between the maximum and minimum intensity. Image noise was calculated by subtracting two images of a static specimen from a third reference image, taking the standard

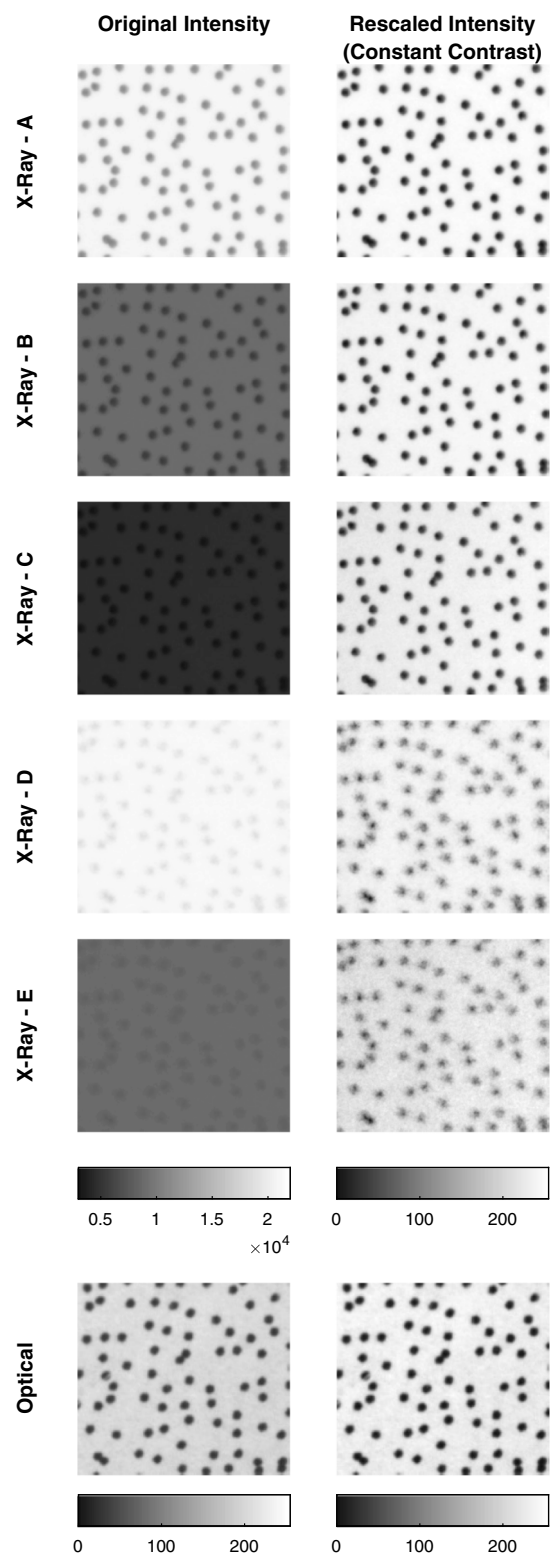
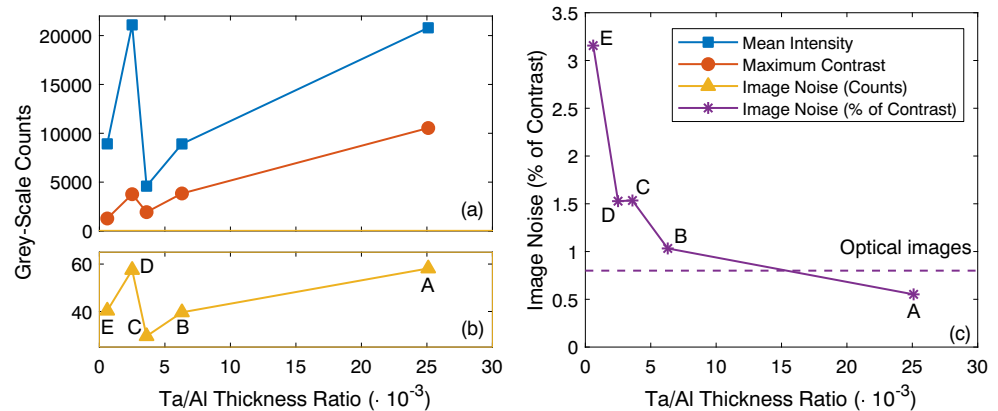


**Fig. 6** Images of a portion of the speckle pattern used for optical DIC and X-ray DIC. The left column shows the actual image intensities, on a reduced range of the 16-bit scale for the X-ray images (3000–22,000 counts), and on the full range of the 8-bit scale for the optical image (0–255 counts). The right column shows the rescaled intensities, such that each image ranges from 0–255 and has constant contrast. Specimen configurations are listed in Table 3

**Fig. 7** Image quality metrics for each of the X-ray specimens. Labels A–E refer to the specimen names, designated in Table 3. (a) Mean intensity, maximum contrast, and image noise, on a 16-bit scale. (b) Magnified region of (a), to show the image noise. (c) Image noise as a percentage of image contrast. The dashed line represents the optical images, for comparison purposes



deviation of the difference, and averaging the standard deviation over two images.

The mean image intensity is driven by the amount of Al the X-rays passed through, where the mean intensity decreases with increasing Al, regardless of the thickness of the Ta speckles. Image contrast is a function of both the thickness of the Ta and the Al, where contrast decreases as the Ta thickness decreases or the Al thickness increases. Image noise, in absolute counts on a 16-bit scale, shows the same trend as the mean intensity, decreasing with increasing Al thickness. Image noise, as a percentage of the contrast, follows the Ta/Al thickness ratio, with noise increasing as the Ta/Al ratio decreases. For comparison, the image noise as a percentage of image contrast was also computed for the optical system, and found to be 0.8%. X-ray specimens A and B have similar or lower noise (0.6% and 1.0%, respectively) compared to the optical system, while the other X-ray specimens have higher noise as a percentage of contrast. The effects of these different image properties on the DIC results are discussed in “Translation Tests”.

## Translation Tests

The images acquired during rigid in-plane and out-of-plane translations of the specimens were correlated

using the DIC parameters described in “DIC Processing Parameters”. The average epipolar error was approximately 0.10 px for the optical images and 0.04 px for the X-ray images, indicating that the calibrations for both imaging systems were satisfactory. The precision and accuracy of the displacements were evaluated as described in “Displacement precision” and “Displacement accuracy”.

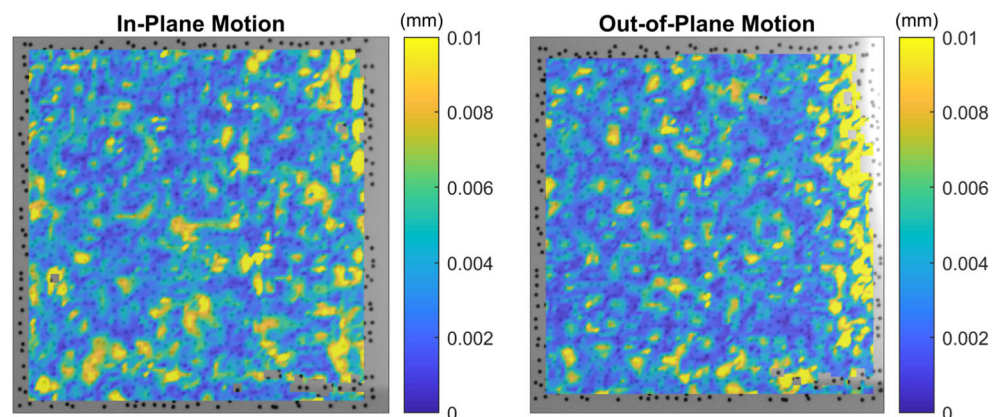
## Displacement precision

To compute the precision, or noise-floor, for the DIC displacements, we first removed rigid body motion using the average transformation for each image. Then, we computed the displacement magnitude,  $D$ , as the Euclidean distance based on the three displacement components,  $U$ ,  $V$ , and  $W$ , as shown in equation (1). By using the displacement magnitude instead of the individual displacement components, we were able to account for any mismatch between the coordinate axes of the optical DIC data, the X-ray DIC data, and the translation stage.

$$D = \sqrt{(U^2 + V^2 + W^2)} \quad (1)$$

Figure 8 presents a contour plot of the displacement magnitude, with rigid body motion removed, for the extreme

**Fig. 8** Contours of the noise residual of the displacement magnitude,  $D$ , with rigid body motion removed, for the extreme in-plane ( $D = 16$  mm) and out-of-plane ( $D = 20$  mm) translations for Specimen C



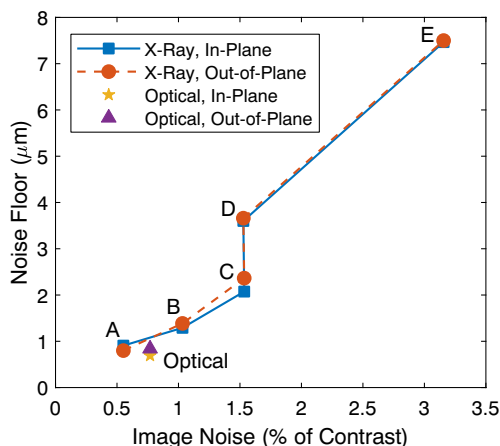


**Fig. 9** Displacement noise floor as a function of image noise (Fig. 7(c)). Labels A–E refer to the specimen names, designated in Table 3

in-plane and out-of-plane translations for Specimen C. With rigid body motion removed, the remaining displacement represents the measurement resolution or noise. The noise pattern is completely random, and there are no obvious spatial bias patterns. This result indicates that the stereo-camera calibration procedure with a pin-hole camera model ([Camera Calibration](#)) is able to adequately describe the stereo X-ray imaging system. Compared to other non-optical imaging techniques used for DIC, such as scanning electron microscopy or atomic force microscopy [33–36], there are no spatial or temporal bias errors that must be corrected. We note, however, that these results could be dependent on the X-ray detector or scintillator that is used; if there are spatial non-uniformities in the detector or scintillator, the images may need to be corrected prior to performing image correlation.

Finally, we computed the standard deviation of  $D$  over the region-of-interest for each image, and then averaged these standard deviations together over all translation steps. This noise-floor analysis takes into account effects of camera noise and also tests the camera calibration and lens distortion correction, since images were taken throughout the entire volume of interest. This is a more complete noise-floor evaluation than if only static images were used, but still represents a minimum noise-floor.

Figure 9 presents the displacement noise-floor as a function of the image noise (Fig. 7c) for the X-ray specimens A–E, as well as for the optical images, for both the in-plane and the out-of-plane translations. There was no significant difference between the noise floor for the in-plane translations compared to that for the out-of-plane translations. The noise-floor for the optical images ranged between 0.7–1.0  $\mu\text{m}$  for the five different tests. Since these five tests all had the same nominal optical image quality, with image noise being approximately 0.8% of the contrast, only the average noise-floor is presented in Fig. 9. Given an image scale of 12.1 px/mm, this noise-floor corresponded to approximately 0.01 px, which is well within the normal noise-floor associated with standard optical DIC measurements.

The noise-floor for the X-ray images varied depending on the specimen, between 0.8–7.5  $\mu\text{m}$ , which corresponded to approximately 0.01–0.12 px with an image scale of 16.4 px/mm. The noise-floor for the different specimens mostly followed the image noise, where specimen A had the lowest image noise (as a percentage of contrast) and the lowest displacement noise-floor, while specimen E had the highest image noise and the highest displacement noise-floor. The jump in the noise floor moving from specimen C to D, even though the image noise remained constant, is

**Fig. 10** Displacement magnitude,  $D$ , from the optical and X-ray DIC results for Specimen C, plotted as a function of applied translation stage displacement. The insets magnify the small displacements of 50  $\mu\text{m}$ . The black line represents a theoretical 1:1 correspondence. The gray arrows and numbers refer to the motion steps described in “Translation Tests”

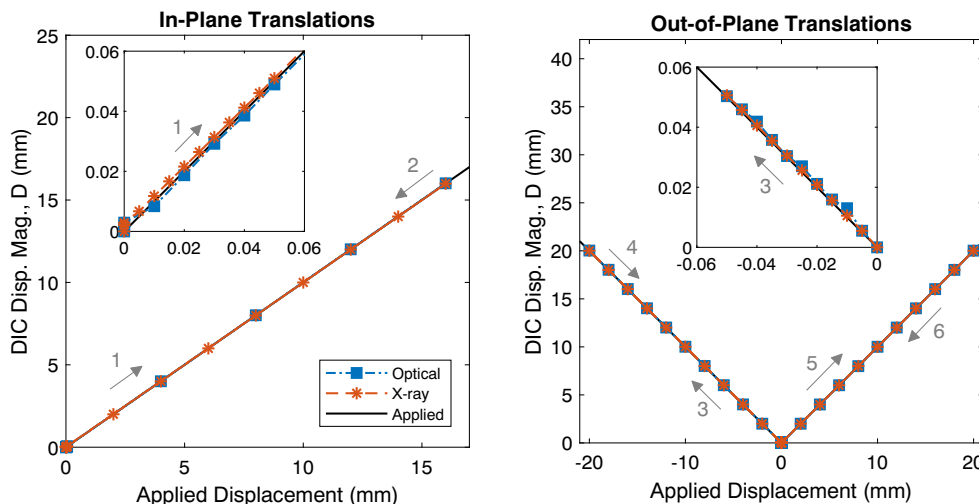


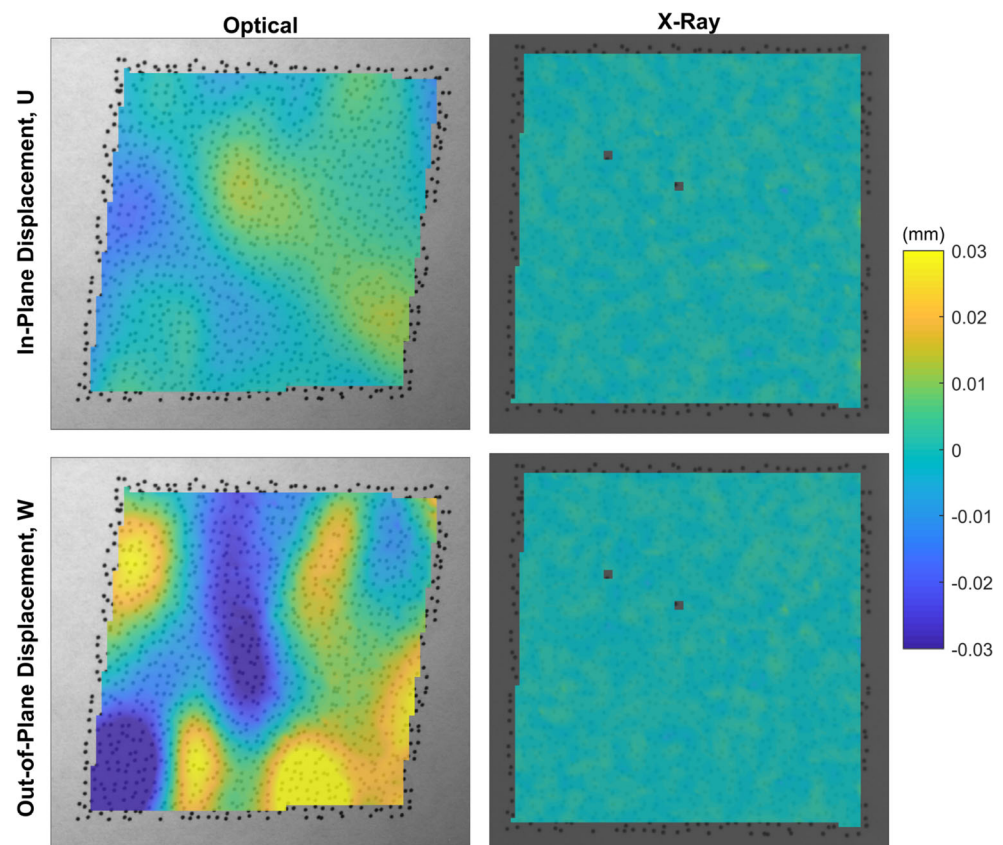
**Table 6** Average error between the DIC displacement magnitude and the translation stage

Specimen	Displacement Error ( $\mu\text{m}$ )			
	In-Plane Disp.		Out-of-Plane Disp.	
	Optical	X-ray	Optical	X-ray
A	3.5	3.2	8.0	3.4
B	3.7	1.4	8.9	5.3
C	3.7	1.5	8.3	6.5
D	3.6	1.7	8.3	3.8
E	4.4	3.3	9.5	4.6

explained by the sharpness of the speckles. Specimen C had  $80\ \mu\text{m}$  thick Ta speckles, which had sharper edges, while Specimen D had  $8\ \mu\text{m}$  thick Ta speckles with fuzzier edges, as shown in Fig. 6. The sharpness of the speckles affected the DIC correlation algorithm, even though both specimens had approximately the same Ta/Al ratio and image noise.

We emphasize that the DIC algorithm is agnostic to the method used to generate the images, e.g. optical imaging versus X-ray imaging. Thus, the X-ray images that had similar image quality and speckle quality as the optical images—specifically specimens A and B—also had comparable displacement resolutions.

**Fig. 11** Contour plots of the in-plane displacement,  $U$  (top row), and out-of-plane displacement,  $W$  (bottom row), for both the optical DIC system (left column) and the X-ray DIC system (right column) for Specimen A, when a hot plate induced heat waves and density gradients in the air between the cameras and the specimen



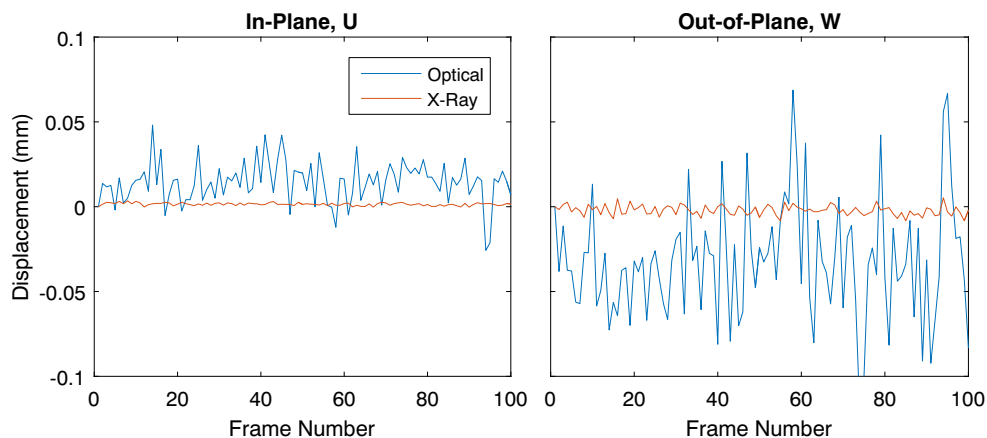
## Displacement accuracy

To evaluate the displacement accuracy of the DIC results, we again computed the displacement magnitude according to equation (1). Here, though, we did *not* remove rigid body motion. The displacement magnitude was averaged over the region-of-interest for each image, and Fig. 10 plots the displacement magnitude from the DIC results as a function of the applied translation stage displacement. Overall, there is very good agreement between the optical DIC measurements, X-ray DIC measurements, and the translation stage, both for small translation steps of less than  $50\ \mu\text{m}$ , as well as for large displacements of  $20\ \text{mm}$ .

The mean errors between the DIC measurements compared to the translation stage displacement (as measured from the optical encoder in the stage), are presented in Table 6. The error of the X-ray DIC measurements is comparable or even lower than the error of the optical DIC measurements for the in-plane displacements. For the out-of-plane displacements, the error for optical DIC was slightly higher ( $8\text{--}9\ \mu\text{m}$ ) than the error for X-ray DIC ( $3\text{--}7\ \mu\text{m}$ ). The cause of this difference is unknown, but since the difference is only a few microns for displacements up to  $\pm 20\ \text{mm}$ , we did not investigate further. Thus we conclude that the X-ray DIC measurements have comparable



**Fig. 12** Displacements of the center subset of the region of interest for Specimen A, when a hot plate induced heat waves and density gradients in the air between the cameras and the specimen



accuracy as the optical DIC measurements for the case of rigid translations investigated in this work.

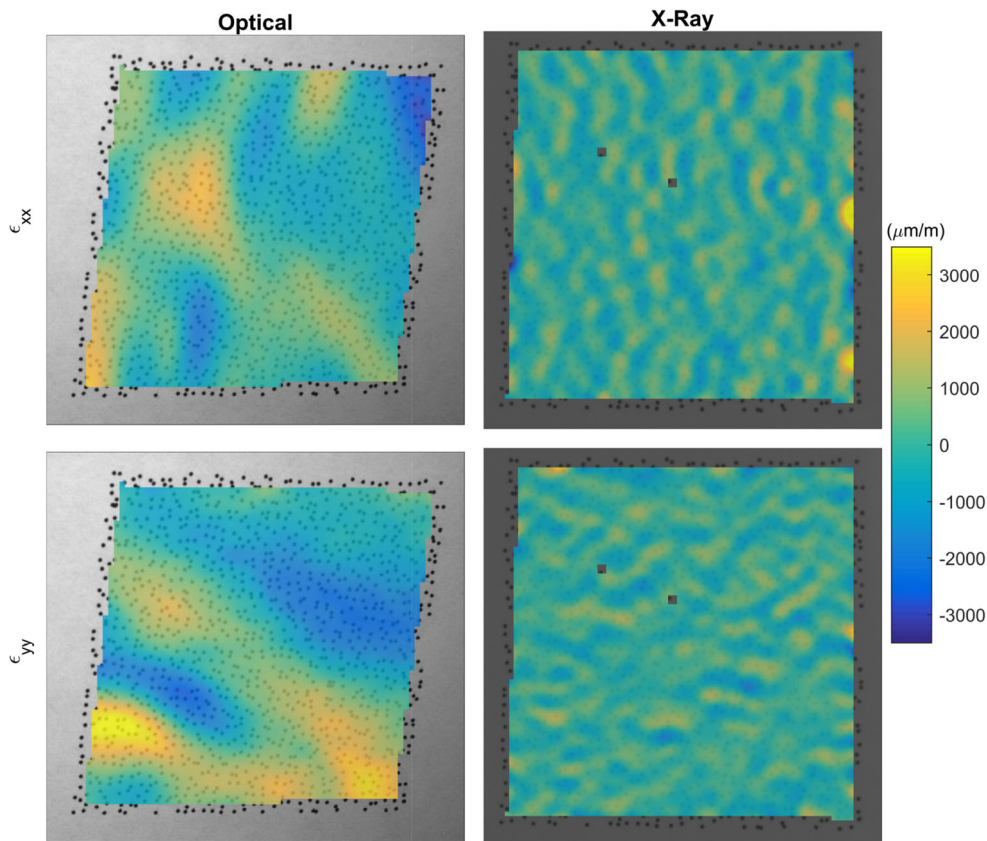
**Hot Plate Tests**

Although it is important to ensure that X-ray DIC does not add significant noise or bias in comparison to optical DIC in standard experimental setups, the primary goal of this work was to evaluate X-ray DIC in the presence of strong air density gradients. To do this, we compared optical DIC with X-ray DIC when a hot plate was situated between

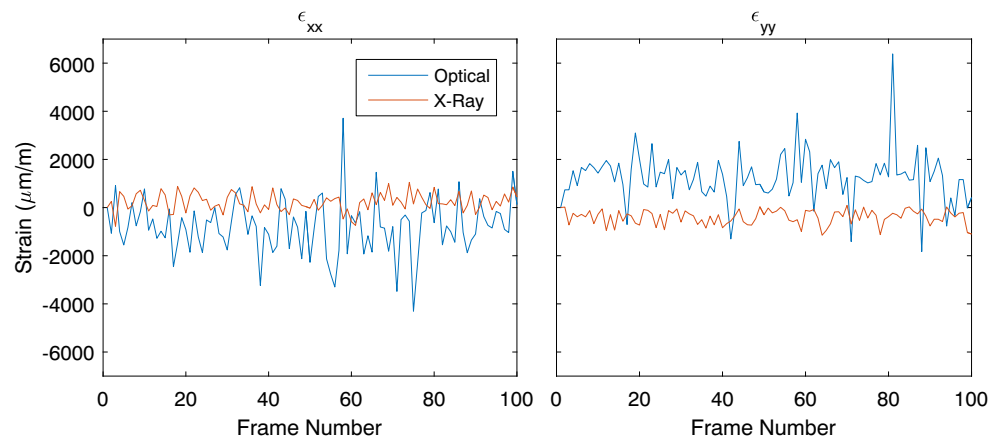
the cameras (and X-ray machines) and the specimen (see Fig. 3). Natural convection developed in the vicinity of the hot plate, creating a volume of air with temperature (and thus density) gradients. Density gradients in the air between the specimen and the optical cameras refract optical light and bias optical DIC measurements [5]; X-rays, however, are not refracted through density gradients in air [14–16].

Figure 11 presents contours of the DIC displacements for Specimen A (Table 3), measured using either the optical system or the X-ray system, when the hot plate was present. Since the specimen was motionless, all measured

**Fig. 13** Contour plots of the horizontal strain,  $\epsilon_{xx}$  (top row), and vertical strain,  $\epsilon_{yy}$  (bottom row), for both the optical DIC system (left column) and the X-ray DIC system (right column) for Specimen A, when a hot plate induced heat waves and density gradients in the air between the cameras and the specimen



**Fig. 14** Normal strains of the center subset of the region of interest for Specimen A, when a hot plate induced heat waves and density gradients in the air between the cameras and the specimen



displacements are errors. The contour plots from the optical system exhibit a large magnitude of displacements as well as the characteristic spatial distribution associated with imaging through heat waves [5]. In contrast, the contour plots from the X-ray system have a lower magnitude of displacements and a distribution characteristic of random noise.

Figure 12 presents the displacements of a single subset in the center of the region of interest as a function of time. Again, we observe that the false displacements in the optical system are significantly larger than the displacements in the X-ray system.

The spatial gradients in the displacements directly induced similar errors in the strain measurements. Figure 13 shows contour plots of the two normal strain components,  $\epsilon_{xx}$  and  $\epsilon_{yy}$ , at the end of the image series, and Fig. 14 shows the strains of the center subset as a function of time.

**Table 7** Spatial and temporal standard deviations of the DIC displacements when a hot plate induced heat waves and density gradients in the air between the cameras and the specimen

	Optical DIC	X-ray DIC	Optical/X-ray ratio
Spatial Standard Deviation of Image 100			
$U$	6.3 $\mu\text{m}$	1.2 $\mu\text{m}$	5x
$V$	9.9 $\mu\text{m}$	1.1 $\mu\text{m}$	9x
$W$	19.9 $\mu\text{m}$	3.9 $\mu\text{m}$	5x
$\epsilon_{xx}$	960 $\mu\text{m/m}$	640 $\mu\text{m/m}$	1.5x
$\epsilon_{yy}$	1320 $\mu\text{m/m}$	490 $\mu\text{m/m}$	2.7x
$\epsilon_{xy}$	820 $\mu\text{m/m}$	400 $\mu\text{m/m}$	2.1x
Temporal Standard Deviation of Center Subset			
$U$	12.2 $\mu\text{m}$	0.8 $\mu\text{m}$	15x
$V$	15.0 $\mu\text{m}$	0.8 $\mu\text{m}$	18x
$W$	34.6 $\mu\text{m}$	2.9 $\mu\text{m}$	12x
$\epsilon_{xx}$	1140 $\mu\text{m/m}$	370 $\mu\text{m/m}$	3.1x
$\epsilon_{yy}$	1040 $\mu\text{m/m}$	310 $\mu\text{m/m}$	3.4x
$\epsilon_{xy}$	940 $\mu\text{m/m}$	270 $\mu\text{m/m}$	3.5x

Just as with the displacements, the X-ray DIC strains have significantly less error than the optical DIC strains. Similar considerations attend the shear strain,  $\epsilon_{xy}$ , as well.

To further quantify the error caused by imaging through heat waves, we computed the spatial standard deviation of the displacements and strains of the contour plots in Figs. 11 and 13. Additionally, we computed the temporal standard deviation of the displacements and strains of the line plots in Figs. 12 and 14. These statistics are presented in Table 7, and are typical results for all time steps and all subsets in the region of interest. The error of the optical DIC displacements was 5–18 times higher than the error of the X-ray DIC measurements, and the error of the optical strains was about 2–3 times higher. These results again show that X-ray-based DIC offers a unique solution to situations where optical-based DIC measurements have significant bias due to refraction.

## Conclusions

In this paper, we presented a novel experimental technique using X-ray imaging for stereo-DIC measurements (XS-DIC). Several methods for generating an appropriate pattern for XS-DIC were evaluated, including applying a mixture of tantalum or tungsten particles on the surface of the specimen by hand, or using thermal spray coating. Thermal spray coating provided the most consistent thickness and controlled location of the speckles, though the manual methods could be refined for situations where thermal spray coating is not available. Relatively thin speckles of tantalum—only 10–80  $\mu\text{m}$  thick—were sufficient to generate high-contrast images, with aluminum specimens up to 22.2 mm thick.

In previous work, we adapted a standard dot-grid calibration target for X-ray imaging. This allowed us to use a standard bundle adjustment process to calibrate the stereo X-ray system. By streamlining the calibration process to

interface directly with commercial DIC software, a major hurdle to using X-ray images for DIC measurements was eliminated.

The noise-floor of XS-DIC displacements ranged from 0.8–7.5  $\mu\text{m}$ , depending on the thickness of the aluminum sample, which compared favorably with the optical S-DIC noise floor of approximately 0.7–1.0  $\mu\text{m}$ . The X-ray image quality and XS-DIC noise-floor are dependent on the specimen material and thickness, and the X-ray source and detector parameters (e.g. accelerating voltage, current, integration time), and would need to be evaluated for each experimental setup. The accuracy and precision of XS-DIC displacements were evaluated from in-plane and out-of-plane rigid translations. The XS-DIC displacements agreed with both the nano-precision stage and simultaneous optical S-DIC displacements, with an average error of only 2–10  $\mu\text{m}$  for applied displacements up to 20 mm.

A hot plate was placed between the specimen and the imaging systems, to induce a heterogeneous index of refraction field, and both optical S-DIC and XS-DIC were used to measure apparent displacements and strains of a static specimen. Optical S-DIC produced false displacements up to 30  $\mu\text{m}$ , while the XS-DIC had errors of only 1–2  $\mu\text{m}$ , leading to a 5–18 times reduction. These spatially-varying false displacements led to strain errors up to 1300  $\mu\text{m}/\text{m}$  for optical S-DIC, but strain errors for XS-DIC were approximately 2–3 times lower.

These results show the power of the X-ray DIC system to provide accurate results of specimen motion and deformation in harsh environments. The focus of the current work was to evaluate XS-DIC in an experimental setup where density gradients in the atmosphere cause significant errors in traditional, optical-based DIC measurements. Our target application is fluid-structure interactions in a shock tube, where imaging through a shock front and turbulent fluid flow induces bias errors in optical DIC of 10–50  $\mu\text{m}$ , the same order of magnitude of the signal of interest. Other situations where density gradients cause beam steering include, for instance, when a specimen is at high-temperature, in a shock or explosive environment, or subjected to complex fluid loading in a wind tunnel. The same XS-DIC technique presented here could also be applied to combustion applications, when the specimen is engulfed in flames or soot and is optically occluded. Additionally, XS-DIC could be leveraged in situations when the specimen of interest is in the interior of an assembly with no optical access. While the current work demonstrated XS-DIC in quasi-static conditions with image acquisition rates of 5 Hz or less, efforts are on-going to extend the technique to high rates of 10–20 kHz. This ability to do high-rate imaging with a continuous X-ray source is critical for dynamic tests, such as in a shock tube, wind tunnel, or explosive environment. Overall, X-ray DIC is a

versatile, non-contact diagnostic, with comparable accuracy and precision as optical DIC, but with unique advantages in situations where optical DIC has significant error or is not feasible.

**Acknowledgments** The authors gratefully acknowledge David Saiz for measurements of the tantalum speckle coating thickness, Andrew Miller and Dr. Andrew Vackel for creating the tantalum speckle pattern using thermal spray, Andrew Lentfer for X-ray imaging and for creating the tungsten speckle pattern using tungsten powder mixed in paint, Paul Farias for creating the drawings of the mask for thermal spray, and Dr. Kyle Lynch and Dr. Benjamin Halls for insightful discussion.

This work was supported by the Laboratory Directed Research and Development program at Sandia National Laboratories, a multimission laboratory managed and operated by National Technology and Engineering Solutions of Sandia, LLC, a wholly owned subsidiary of Honeywell International Inc., for the U.S. Department of Energy's National Nuclear Security Administration under contract DE-NA0003525. This paper describes objective technical results and analysis. Any subjective views or opinions that might be expressed in the paper do not necessarily represent the views of the U.S. Department of Energy or the United States Government.

## Compliance with Ethical Standards

**Conflict of Interest** On behalf of all authors, the corresponding author states that there is no conflict of interest.

## References

- Sutton MA, Orteu JJ, Schreier H (2009) Image correlation for shape, motion, and deformation measurements: basic concepts, theory, and applications. Springer US
- Sutton MA, Wolters WJ, Peters WH, Ranson WF, McNeill SR (1983) Determination of displacements using an improved digital correlation method. *Image Vision Comput* 1(3):133–139
- International Digital Image Correlation Society, Jones EMC, Iadicola MA (2018) A good practices guide for digital image correlation, 1 edn. <https://doi.org/10.32720/idics/gpg.ed1>
- Smith CM, Hoehler MS (2018) Imaging through fire using narrow-spectrum illumination. *Fire Technol* 54:1705–1723
- Jones EMC, Reu P (2018) Distortion of digital image correlation (DIC) displacements and strains from heat waves. *Exp Mech* 58:1133–1159
- Abotula S, Heeder N, Chona R, Shukla A (2014) Dynamic thermo-mechanical response of Hastelloy X to shock wave loading. *Exp Mech* 54:279–291
- Pan B, Wu D, Wang Z, Xia Y (2011) High-temperature digital image correlation method for full-field deformation measurement at 1200c. *Meas Sci Technol* 22:1–11
- Gupta S, Parameswaran V, Sutton MA, Shukla A (2014) Study of dynamic underwater implosion mechanics using digital image correlation. *Proc R Soc A* 470:1–17
- Reu P, Miller TJ (2008) The application of high-speed digital image correlation. *J Strain Anal* 43:673–688
- Pankow M, Justusson B, Waas AM (2010) Three-dimensional digital image correlation technique using single high-speed camera for measuring large out-of-plane displacements at high framing rates. *Appl Opt* 49(17):3418–3427
- Lynch KP, Jones EMC, Wagner JL (2018) Simultaneous PSP and surface deformation measurements for fluid-structure interactions



- in a shock tube. In: 2018 fluid dynamics conference, AIAA AVIATION forum. AIAA, pp 2018–3870
12. Giovannetti LM, Banks J, Turnock SR, Boyd SW (2017) Uncertainty assessment of coupled digital image correlation and particle image velocimetry for fluid-structure interaction wind tunnel experiments. *J Fluid Struct* 68:125–140
  13. Spottswood SM, Bebernis TJ, Eason TG, Perez RA, Donbar JM, Ehrhardt DA, Riley ZB (2018) Exploring the response of a thin, flexible panel to shock-turbulent boundary-layer interactions. *J Sound Vib*. <https://doi.org/10.1016/j.jsv.2018.11.035>
  14. Henke BL, Guillikson EM, Davis JC (1993) X-ray interactions: photoabsorption, scattering, transmission, and reflection at  $E = 50\text{--}30,000$  eV,  $Z = 1\text{--}92$ . *Atom Data Nucl Data* 54:181–342
  15. Thompson A, Attwood D, Guillikson EM, Howells M, Kim K-J, Kirz J, Kortright J, Lindau I, Liu Y, Pianetta P, Robinson A, Scofield J, Underwood J, Williams G, Winick H (2009) X-ray data booklet. Available online: <http://xdb.lbl.gov/>. Accessed 2018-05-10. National Lawrence Berkeley National Laboratory
  16. Chantler CT, Olsen K, Dragoset RA, Chang J, Kishore AR, Kotochigova SA, Zucker DS (2000) X-ray form factor, attenuation and scattering tables, 2005. Version 2.1. Available online: <http://physics.nist.gov/ffast>. Accessed 2018-05-10. National Institute of Standards and Technology, Gaithersburg, MD. Originally published as Chantler, C.T., *J. Phys. Chem. Ref. Data* 29(4), 597–1048 (2000); and Chantler, C.T., *J. Phys. Chem. Ref. Data* 24, 71–643 (1995)
  17. Hubbell JH, Seltzer SM (2018) X-ray mass attenuation coefficients. NIST Standard Reference Database 126. <https://www.nist.gov/pml/x-ray-mass-attenuation-coefficients> Accessed Nov 2018
  18. Russell SS, Sutton MA (1989) Strain-field analysis acquired through correlation of X-ray radiographs of a fiber-reinforced composite laminate. *Exp Mech* 29(2):237–240
  19. Synnergren P, Goldrein HT, Proud WG (1999) Application of digital speckle photography to flash x-ray studies of internal deformation fields in impact experiments. *Appl Opt* 38(19):4030–4036
  20. Prentice HJ, Proud WG, Walley SM, Field JE (2010) The use of digital speckle radiography to study the ballistic deformation of a polymer bounded sugar (an explosive simulant). *Int J Impact Eng* 37:1113–1120
  21. Grantham SG, Goldrein HT, Proud WG, Field JE (2003) Digital speckle radiography—a new ballistic measurement technique. *Imaging Sci J* 51(3):175–186
  22. Rae PJ, Williamson DM, Addiss J (2011) A comparison of 3 digital image correlation techniques on necessarily suboptimal random patterns recorded by x-ray. *Exp Mech* 51(4):467–477
  23. Louis L, Wong T-F, Baud P (2007) Imaging strain localization by X-ray radiography and digital image correlation: deformation bands in Rothbach sandstone. *J Struct Geol* 29:129–140
  24. Bay BK (1995) Texture correlation: a method for the measurement of detailed strain distributions within trabecular bone. *J Orthop Res* 13:258–267
  25. Synnergren P, Goldrein HT (1999) Dynamic measurements of internal three-dimensional displacement fields with digital speckle photography and flash x-rays. *Appl Opt* 38(28):5956–5961
  26. Bay BK, Smith TS, Fyhrie DP, Saad M (1999) Digital volume correlation: three-dimensional strain mapping using x-ray tomography. *Exp Mech* 39(3):217–226
  27. Bay BK (2008) Methods and applications of digital volume correlation. *J Strain Anal* 43:745–760
  28. Croom BP, Jin H, Mills B, Li X (2019) Effect of fragile speckle patterns on accuracy of digital volume correlation. *Exp Mech*. <https://doi.org/10.1007/s11340-019-00512-4>
  29. An introduction to thermal spray. BRO-0005.6, 2016. Available online: <https://www.oerlikon.com/metco/en/products-services/coating-equipment/thermal-spray/processes/>. Accessed 2018-05-10. Oerlikon Metco
  30. Davis JR (2004) Handbook of thermal spray technology. ASM International
  31. Reu P (2014) All about speckles: speckle size measurement. *Exp Tech* 38(6):1–2
  32. Miller TJ, Quintana EC (2013) Stereo x-ray system calibration for three-dimensional measurements. Available online: <https://prod.sandia.gov/techlib/auth-required.cgi/2013/132097c.pdf>. Accessed 2018-05-10
  33. Li N, Sutton MA, Li X, Schreier HW (2008) Full-field thermal deformation measurements in a scanning electron microscope by 2d digital image correlation. *Exp Mech* 48(5):635–646
  34. Xu Z-H, Li X-D, Sutton MA, Li N (2008) Drift and spatial distortion elimination in atomic force microscopy images by the digital image correlation technique. *J Strain Anal Eng* 43(8):729–743
  35. Zhu T, Sutton MA, Li N, Orteu JJ, Cornille N, Li X, Reynolds AP (2011) Quantitative stereovision in a scanning electron microscope. *Exp Mech* 51(1):97–109
  36. Maraghechi S, Hoefnagels JPM, Peerlings RHJ, Rokoš O, Geers MGD (2019) Correction of scanning electron microscope imaging artifacts in a novel digital image correlation framework. *Exp Mech* 59(4):489–516

**Publisher's Note** Springer Nature remains neutral with regard to jurisdictional claims in published maps and institutional affiliations.

